Physics and Chemistry of Minerals (2019) 46:959–975
https://doi.org/10.1007/s00269-019-01055-9

ORIGINAL PAPER

Defects in deformation twins in plagioclase

Dongyue Xie[1] · Greg Hirth[2] · J. P. Hirth[3] · Jian Wang[1]

Received: 5 July 2019 / Accepted: 23 September 2019 / Published online: 10 October 2019

Abstract
The topological model is applied to analyze defects associated with albite and pericline twins in plagioclase. Twin growth occurs by the motion of twinning disconnections. The same twinning disconnections are shown to produce both twins. The topological model is used to predict the atomic details of the disconnections. High-resolution transmission electron microscopy results verify the model predictions. Early work on the possibility of pseudo-twinning is also discussed.

Keywords Twinning · Mineral · Structural group · Dislocations · Disconnections · Topological model

Introduction

Twinning is ubiquitous in minerals. Indeed, the understanding of twinning originated with early work by Mügge (1889) and other mineralogists as reviewed by Duparc (2017). It is prominent in deformed plagioclase minerals. While twinning has been understood macroscopically for more than a century, atomic scale descriptions are still being developed. Early work (Bevis and Crocker 1969; Bilby and Crocker 1965; Frank 1951) established twinning dislocations as the defects causing deformation twin growth and highlighted the need for atom shuffling in some cases (Bevis and Crocker 1969). These ideas are reviewed in Christian and Mahajan (1995) and Kelly and Knowles (2012). More recently, in the topological model (TM) (Pond et al. 2007), the defects have been defined as twinning disconnections (TDs) to emphasize the importance of the step height. Disconnections are line defects resembling dislocations, but have the added feature of a step. They are characterized by the step height *h* and the Burgers vector ***b*** of any dislocation content. Figure 1 shows how a disconnection can be created from two crystals with surface steps. For twinning, the Burgers vector is parallel to the low index surfaces that join to form a coherent terrace plane (dashed red vector). The glide plane on which a disconnection glides is the same as that of the component dislocation. An illustration of such a disconnection with dislocation content in Fig. 1c indicates the strain field, shear and step associated with the disconnection. When the disconnection glides, one can imagine that the partial dislocation moves first, producing shear and translating the interface by *h*, leaving what is tantamount to a stacking fault in its wake. Shuffles then occur, thermally activated or athermally, to remove the fault and restore the perfect twin interface.

These characteristics are formally defined in reference crystallographic spaces in the TM, recently reviewed in Hirth et al. (2013); the TM also applies to phase transformation, grain boundary characterization and other physical phenomena. The TM for deformation twinning is reviewed in Hirth et al. (2016) and for recovered twins and annealing/growth twins is considered in Gong et al. (2017). Most of the atomic scale theories, atomistic models and high-resolution transmission electron microscopy (HRTEM) observations have been for metals. In a companion paper (Hirth et al. 2019), we presented some added concepts within the TM that facilitate the description of disconnections in complex minerals, i.e., those with many atoms in their unit cell.

Here, we apply the TM to analyze twins in two plagioclase feldspars: a relatively pure albite (An_{01}) that formed in a pegmatite (Tanco albite) and a deformed labradorite (An_{60}) from an oceanic gabbro (Mehl and Hirth 2008). The two samples are of interest because they exhibit a range of microstructures that are interpreted to indicate nominally low stress conditions with little deformation (Tanco albite)

✉ Jian Wang
jianwang@unl.edu

[1] Mechanical and Materials Engineering Department, University of Nebraska-Lincoln, Lincoln NE68588, USA

[2] Department of Geological Sciences, Brown University, Providence, RI 02912, USA

[3] Ohio State and Washington State Universities, 546 S. Park Centre Ave, Green Valley, AZ 54614, USA

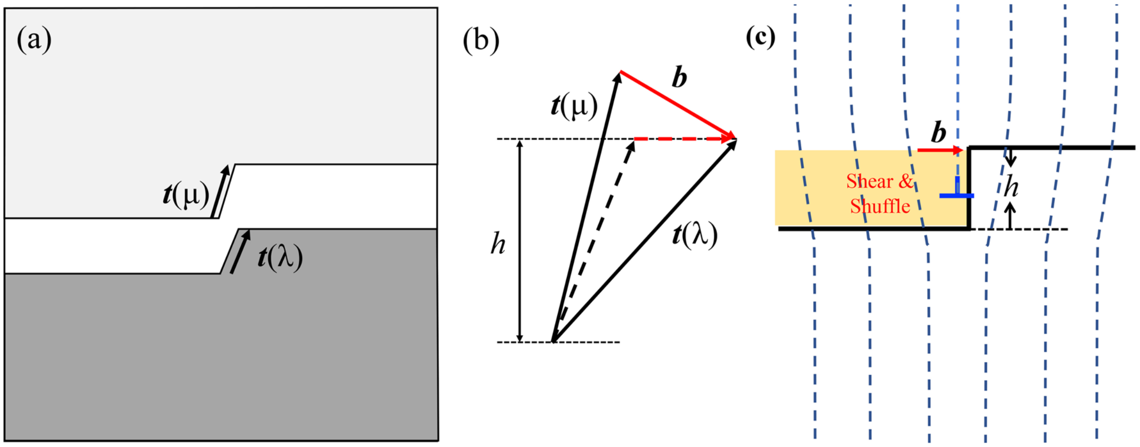

Fig. 1 **a**, **b** Schematic diagram of a disconnection formed by bonding crystals λ and μ at an incompatible step. The height of a disconnection is denoted as h. The Burgers vector $\boldsymbol{b}$ is the difference between the two translation vectors. In the twinning case, step heights are the same in the two crystals, the Burgers vector and the translation vector $\boldsymbol{t}$(μ) are indicated by the dashed arrows. **c** Resultant disconnection

and higher stress conditions and more rapid cooling resulting from deformation in the oceanic lithosphere (oceanic gabbro). The Tanco albite is from the marginal zone of the Tanco pegmatite, Ontario; the rock is almost pure albite, with 1% apatite and trace amounts of muscovite. The sample we used shows randomly oriented lathe-shaped grains, indicating little deformation occurred after the pegmatite crystallized (Tullis et al. 1998). The oceanic gabbro was collected in Ocean Drilling Program Hole 735B. These samples of crustal gabbro formed at the Southwest Indian Ridge, experience stresses of 20–100 MPa during deformation at temperature of 700–850 °C, and then cooled rapidly preserving the high temperature deformation microstructures (Mehl and Hirth 2008).

The major twins in these crystals, albite twins and pericline twins, are well understood macroscopically. Understanding the defects in these specimens can help resolve issues related to the differences in stress and the time scales for twinning in the laboratory and the earth. The time scale for atomistic simulations is of the order of a factor of 10^8 shorter than those in laboratory deformations (Van Swygenhoven and Derlet 2008), which are, in turn, approximately 10^8 shorter than those relevant for natural deformation of plagioclase. Simulation results agree with those found in laboratory studies in metals (Hirth et al. 2016), demonstrating that laboratory and natural specimens have similar defect structures that would indicate that similar mechanisms of twinning occur, despite the difference in time scale.

Our purpose here is to examine the twins in plagioclase at the atomistic scale to verify the presence of TDs, postulated to be the defects responsible for twin growth. Twin boundaries in both specimens are studied by HRTEM to determine the TD structure, and then described by the TM. In the following sections, we: (a) first consider macroscopic effects of twins in plagioclase in Sect. 2; (b) review concepts of the TM and analyze the components of twinning disconnections including step height, Burgers vector and shuffle vectors in Sect. 3; and (c) present HRTEM observations regarding TDs predicted by the TM in Sect. 4.

Macroscopic phenomena

The familiar albite and less common pericline twinning systems in plagioclase are known to be a type I and a type II twins, respectively, as distinguished by their crystallographic twinning elements (Li and Knowles (2013). The classical nomenclature for twinning elements (twin plane and twinning direction and angle between them) is reviewed by Hardouin Duparc (2017) and illustrated in Fig. 2. For a type I twin, the primary (K_1) plane (twin plane) is the invariant plane of simple (engineering) shear that contains the twinning (shearing) direction (η_1). There is a second invariant plane (K_2) that contains the twinning direction (η_2), comprising what are called the conjugate or reciprocal twin parameters. For type I twins, K_1 and η_2 have rational indices and K_2 and η_1 have irrational indices. The twin axis ($\boldsymbol{n}$) is normal to the shear plane (p) which contains the two twinning directions (Duparc 2017). In contrast, for type II twins, K_1 and η_2 have irrational indices and K_2 and η_1 have rational indices. In compound twins, common in metals but rare in minerals, all elements are rational. To avoid confusion in scenarios where both the primary and conjugate twins are present in plagioclase, the elements of the type II twin (e.g., a pericline twin) are denoted with prime symbols, such that K_1' (pericline) = K_2 (albite); K_2' (pericline) = K_1 (albite); η_1'(pericline) = η_2 (albite); η_2' (pericline) = η_1 (albite). Twin indices are

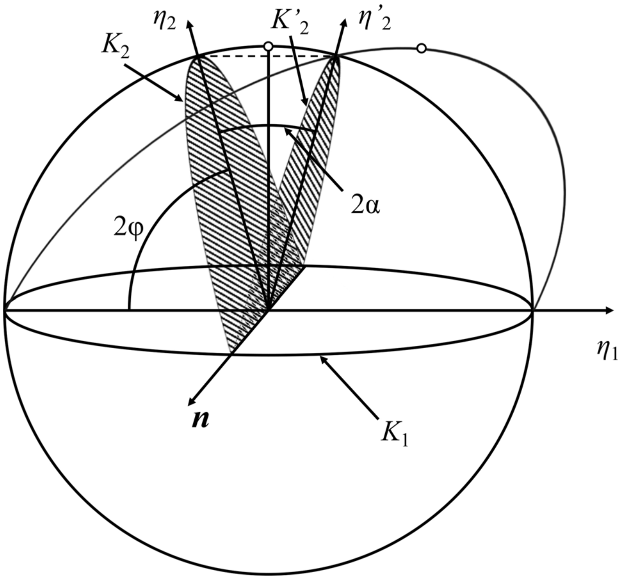

Fig. 2 Schematic of macroscopic twinning elements. (Hardouin Duparc 2017)

identified as $[hkl]_T$ and the rotated planes in the twin are K_1^T and K_2^T. The angle between K_1 and K_1^T is 2 α and the angle between K_1 and K_2 is 2 φ, the complement of α (Fig. 2).

Mechanistically, as discussed in the next section, the glide plane for TDs for type I twins is the K_1 plane, while for type II twins the glide plane is K_2. To separate defect-scale descriptions from macroscopic descriptions, the TM follows the Frank notation (Frank 1953) in identifying the disconnection glide plane as k_1 and the glide direction as γ_1 with k_2 and γ_2 for the conjugates. Thus, for a type I twin $K_1 \equiv k_1$, $K_2 \equiv k_2$, $\eta_1 \equiv \gamma_1$, and $\eta_2 \equiv \gamma_2$. In contrast, for a type II twin in the TM (Pond and Hirth 2018; Pond et al. 2019), $K_1 \equiv k_2$, $K_2 \equiv k_1$, $\eta_1 \equiv \gamma_2$, and $\eta_2 \equiv \gamma_1$. The twinning elements for the albite and pericline twins are presented in Table 1.

A micrograph of twinned labradorite from the oceanic gabbro specimen is shown in Fig. 3. Large type I albite twins with $K_1 = (010)$ are depicted. These are of interest because twin barriers, such as defect interactions, and blockage of twins should be less likely under low stress/low strain rate conditions, so that twins can grow to large size relatively unimpeded as compared to those formed at high stress/high strain-rate in the laboratory (e.g., Stünitz et al. 2003). Also present are finer type I albite twins that presumably formed at lower temperatures. In addition, there are finer type II pericline twins that are conjugates that have the same sense of twin rotation (as indicated by their common extinction in the micrograph). The features in this figure closely resemble micrographs of twinning in Mg (see Sect. 10 of Hirth et al. 2016). Figure 3c shows the twins that were analyzed in HRTEM and identified as albite and pericline twins. Figure 3b shows changes in contrast at twin crossings (solid arrow) and interactions as twins approach one another (dashed arrow).

Although the conjugate albite and pericline twins produce the same twin rotation, they have rotational incompatibilities

Table 1 Twinning elements characteristic for twins in low albite and labradorite

Twinning mode	Mineral	K_1	K_2	η_1	η_2	γ
Albite	Labradorite	(010)	(− 1, 0, 38.33)	[1, 0, 2.718]	[010]	0.136
Pericline	Labradorite	(− 1, 0, 38.33)	(010)	[010]	[1, 0, 2.718]	0.136
Albite	Low Albite	(010)	(1, 0, − 1.587)	[− 1, 0, 8.057]	[010]	0.148

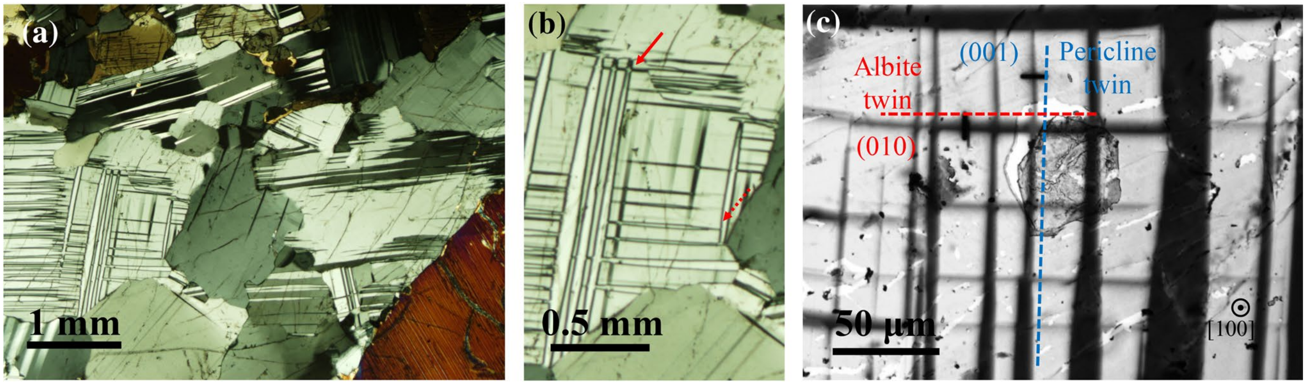

Fig. 3 **a** Cross-polarized light micrograph of deformed labradorite showing deformation twins with different modes. **b** Arrow indicates blocking at an intersection. **c** Albite and pericline twins are identified. Small dark rectangles are FIB cuts

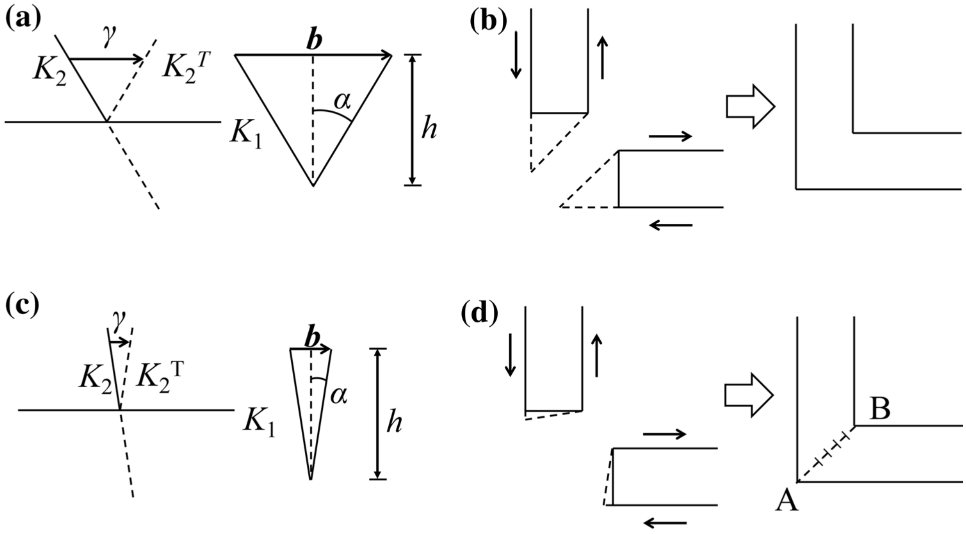

Fig. 4 **a** Classical description of a twin. **b** Paired twin systems with $\alpha = 45^\circ$, in a crystal, shearing to the dashed configuration. **c** Equivalent of **a** for low albite. **d** Equivalent of **b** for low albite. Incompatibility leads to a tilt wall A–B at the intersection

where they intersect. The essence of the compatibility problem is illustrated schematically in Fig. 4. A conjugate system with a large shear is shown in Fig. 4a, with an insert relating the shear to disconnection properties Fig. 4b shows a macroscopic engineering shear γ of unity, producing a displacement angle of 45°, on both the primary and conjugate systems. Together, these shears are completely compatible, and the twin has an "elbow" configuration with no defects at the intersection. Twins of this type have been observed in compound twinning systems in hexagonal close-packed (*hcp*) crystals where K_1 and K_2 are nearly orthogonal (Xu et al. 2019). In face centered cubic (*fcc*) crystals, the compound twins are not orthogonal but the shear is still large. There is then an incompatibility, and a higher-order twin boundary: e.g., a $\{221\}$ twin boundary, forms where two $\{111\}$ twin boundaries meet in fcc crystals. In general, when twins intersect, they form boundaries, such as the $\{221\}$ boundary, comprised of partial dislocations at the intersection (Hirth et al. 2016; Yu et al. 2014a, b; Zhu et al. 2009); these are conventionally called stair-rod partials (Anderson et al. 2017). For albite, the shears are relatively small (see Fig. 4c). This also produces an incompatibility at the intersection, Fig. 4d. The incompatibility leads to a repulsion as a pericline twin approaches an albite twin, or vice versa, consistent with the observation in Fig. 3b, where intersecting twins tend to be pinched off as they near a previously formed twin boundary. If one twin translates through the other, conjugate pair twin configurations similar to those in Fig. 3 are called "cross twins, cyclical twins, or contact twins" in minerals (Smith 1974), while in metals they are called "X", "Y" and "V" (Zhu et al. 2009). Where they cross, a region is doubly twinned, and there are differing rotations (e.g., Hahn and Klapper 2006), reflected by the change in contrast at the intersections observed in cross-polarized light micrographs (e.g., Fig. 3b). While other secondary twins are possible in plagioclase, most twins are either the type I primary or type II conjugate twins discussed above and we restrict the analysis mainly to these.

Topological model

Twinning disconnections

A detailed analysis of the TD characteristics for plagioclase is given in Hirth et al. (2019), and summarized briefly here. As shown in Fig. 1, the TDs are characterized by a Burgers vector $\boldsymbol{b}$ and a step height h; for twins, step heights like those shown in Fig. 1a would be the same for the matrix and the twin. Motion of the TD produces the growth of the twin. The characteristics are displayed in a coherent (also called commensurate) dichromatic pattern (CDP), the superposition of the perfect twin and matrix crystal was aligned in the twin orientation so that they are commensurate on the twin plane. As an example, Fig. 5 shows the CDP for a $\{301\}$ twin in *fcc*. The Burgers vector is expressed by

$$\boldsymbol{b} = \boldsymbol{t}(\lambda) - \boldsymbol{t}(\mu) \qquad (1)$$

where $\mathbf{t}(\boldsymbol{\lambda})$ and $\mathbf{t}(\mu)$ are translation vectors of the matrix μ and the twin λ, respectively, in the CDP. The step height (h) is defined by

$$h = ih_0 = id \qquad (2)$$

where h_0 is the step height of a unit disconnection, equal to the d-spacing parallel to the twin plane, and the integer i is the number of planes comprising the step. The unit disconnection, that with minimum possible step height, has $i = 1$. Passage of a disconnection produces an engineering strain

$$\gamma = b/h \qquad (3)$$

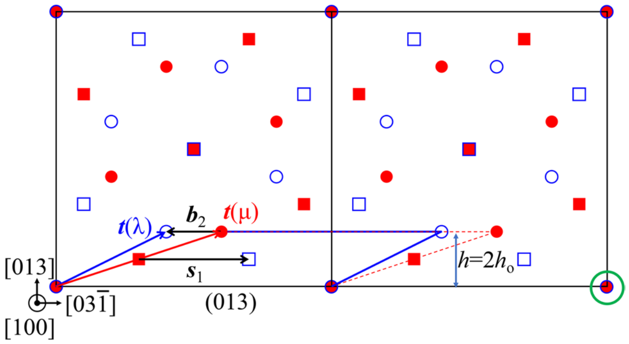

Fig. 5 Coherent dichromatic complex of a (103) twin in *fcc* crystals (Hirth et al. 2016). Red sites represent the matrix and open sites represent the twin. Circles and squares are at different levels in the [100] direction. Matrix and twin sites coincide on the twin plane. Subscripts indicate the level of the plane

In addition, particularly when $i > 1$, local atomic displacements called shuffles (which produce no plastic strain) are required to complete the transformation. Shuffles are characterized in the coherent dichromatic complex (CDC), the superposition of the twin and matrix crystal structures, including the local atomic motif, aligned so that they are coherent on the twin plane. The shuffle vectors, $\boldsymbol{s}$, are defined in terms of the relative displacements of $\boldsymbol{u}(\lambda)$ and $\boldsymbol{u}(\mu)$ in the CDC as shown in Fig. 5

$$\boldsymbol{s} = \boldsymbol{u}(\lambda) - \boldsymbol{u}(\mu) - \boldsymbol{b} \tag{4}$$

For simple structures like *fcc*, the CDC is uncomplicated and the determination of Burgers vectors and shuffle vectors is straightforward. For complex structures like albite, the Burgers vector is easy to determine but the shuffles would be extremely difficult to find from an analog of Fig. 3. Instead, shuffles are more easily found by identifying reduced sets of atoms called structural groups, as discussed in detail in Hirth et al. (2019). These groups are described in the next section.

Crystal structure

Plagioclase is a group of feldspars with a solid solution between albite ($NaAlSi_3O_8$) and anorthite ($CaAl_2Si_2O_8$). For low albite, the conventional unit cell (Hahn and Klapper 2006; Smith 1974; Wenk and Bulakh 2016) is shown in Fig. 6a. The cell is composed of silicon and aluminum centered in oxygen tetrahedra, with sodium and calcium atoms located at the interstices. The unit cell contains 52 atoms, four times the chemical formula. The structure is triclinic with a basis of two and a center of inversion symmetry. The symmetry of the point group is Ci and that of the space group is $C\bar{1}/P\bar{1}$ (Smith and Brown 2012). There is a smaller Niggli cell (Niggli 1928; Santoro and Mighell 1970) that is primitive triclinic and more practical to use in the TM (see Fig. 2 of Hirth et al. 2019). However, we use the conventional unit cell in Fig. 6a in order to agree with the conventional usage (Hahn and Klapper 2006; Smith 1974; Wenk and Bulakh 2016). One must notice that the base-centered site on the (001) plane is a lattice site. Indeed, the formal description of the unit cell in Fig. 6a would be base-centered triclinic. Thus, the *d*-spacing is half that of the (010) planes, i.e., the (020) planes in Fig. 6a. The lattice parameters of low albite (Harlow and Brown 1980) and labradorite (Horst et al. 1981) are listed in Table 2.

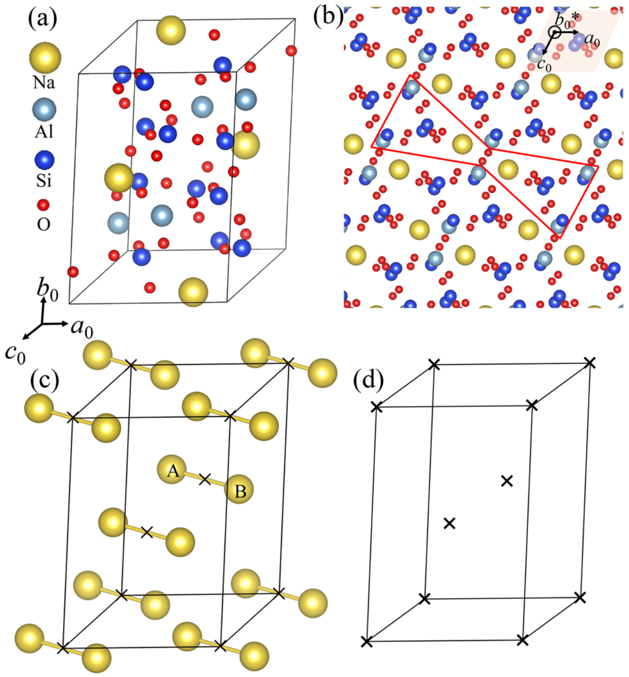

Fig. 6 **a** Conventional unit cell of albite. **b** Atomic motif at a lattice site in albite (Hirth et al. 2019). **c** Unit cell showing structural group dipoles A–B at lattice sites. **d** Corresponding crystal lattice

Each lattice site has an associated atomic motif as represented in Fig. 6b. It is very difficult to analyze the atomic shuffle motions accompanying disconnection motion from such a figure. The shuffle analysis can be greatly simplified, as described subsequently in Sect. 3.2.3, if one describes each atomic motif as a structural group dipole A–B, Fig. 6c. The concept of such groups was implied in Li and Knowles (2013) and formally described in Hirth et al. (2019). A structural group dipole includes all atoms related by the point-group symmetry. The groups are space filling and each group resembles a Voronoi polyhedron (the smallest space-filling volume created by planes constructed perpendicular to and bisecting pairs of lattice sites). From the point group symmetry, each atomic site in one group member of the structural group dipole has inversion symmetry with respect to a site on the other side of the structural group dipole (see Hirth et al. 2019). For albite, the Na atoms are

Table 2 Lattice parameters of labradorite and low albite in nm and degrees

Mineral	Space group	a_0	b_0	c_0	α_0	β_0	γ_0
Labradorite	$C\bar{1}$	0.8178	1.2865	0.7109	93.53	116.21	89.92
Low Albite	$C\bar{1}$	0.8142	1.2785	0.7159	94.19	116.61	87.68

the logical reference site for the group; they show the dipole rotations relative to the crystal axes, and they are the only atoms in the group that, mechanistically, are simply rotated during twinning (i.e., no Na shuffles are required to complete the transformation). Each dipole has a Na–Na spacing of 0.392 nm, is inclined to the (010) plane by $\beta_1 = 4.2°$, and the (010) plane is inclined to the [100] direction by $\beta_2 = 2.4°$. Figure 6d shows the corresponding crystal lattice that is the foundation for the CDP. We next analyze the Burgers vector (whose motion describes the twinning shear) and the shuffles (atomic motions necessary to move all atoms into positions required by mirror symmetry) for the twins.

Disconnections in twins

Disconnections for type I albite and type II pericline twins in plagioclase are schematically illustrated in Fig. 7; a detailed analysis for type II twins in general is presented in Pond and Hirth (2018) and Pond et al. (2019). Type II pericline twins have the same k_1 glide plane and the same γ_1 glide direction, parallel to $\boldsymbol{b}$, as the type I twin, an unusual if not unique inter-relation. In both twin types, the disconnections produce the same simple shear. For type II pericline twins, the rotation associated with the shear must be partitioned between the matrix and the twin to satisfy elastic equilibrium. As discussed in Pond et al. (2019), the neglect of this partitioning requirement led to some inconsistencies in the classical models. However, the TM shows that the rotation 2α is partitioned equally to the matrix and twin. After the combination of disconnection shear and accommodational rotation, the type II twin is precisely the conjugate of the type I twin. The shear directions for both types of twins are favored by the Peach–Koehler forces (Anderson et al. 2017) produced by resolved shear stresses on the twin plane, which act on the disconnections and cause them glide under most loading conditions. The Peach–Koehler forces acting on TDs associated with both types of twins are in general different unless their twin planes are perpendicular.

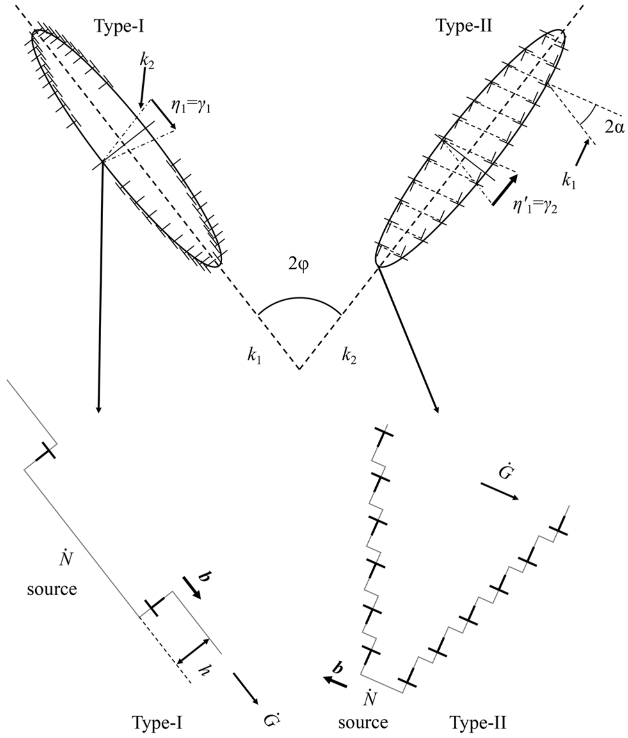

Fig. 7 Schematic illustration of the topological model for the formation of type I albite and type II pericline twins. The shear plane p (which contains both γ_1 and γ_2) is parallel to the page, and is irrational. Sources for the nucleation of a disconnection pair operate on the disconnection glide plane, k_1, in both cases, as indicated by the inset sketches, producing the simple shear displacement parallel to the relevant twin direction. After relaxation, the k_1 planes within the type II twin are rotated by an angle α from their original orientation. The notation Ń indicates a repeated nucleation site. For type I, the mobility/nucleation rate ratio $\dot{G}/\dot{N}$ is large so the spacing L of a pair is large when a new pair nucleates at the source. For type II, the ratio is small when a new pair nucleates and interactions of the dislocation components tends to form a tilt wall, which rotates the wall by α to the final k_2 position

As shown in Fig. 7, twin formation involves the nucleation (at a source) and growth (by glide of TDs). When the disconnection has a high ratio of glide mobility, $\dot{G}$, to nucleation rate, $\dot{N}$, a type I twin forms directly. With a large $G/\dot{N}$ ratio, a nucleated defect pair is widely separated when the next pair nucleates and a type I twin is formed. With a small $G/\dot{N}$ ratio, the separation of the first pair is small and a type II twin is formed. Thus, type II twins become more likely if the ratio is sufficiently small. Consequently, the disconnections accumulate into a tilt wall (which makes them less mobile), and the twin boundary forms on an irrational k_2 plane, with accommodational relaxation producing a rotation of the wall. The unusual case for plagioclase is that both the type I and II twins can form with identical TDs (we know of no prior example). Thus, for type-II pericline twinning, the topological disconnection parameters are the same as those for type I albite twinning, as shown in Fig. 7.

Since the actual CDP for albite is difficult to envision, we first present the simpler case where $\boldsymbol{b}$ is parallel to [001]. As seen in Fig. 8, the $\boldsymbol{t}$ vectors lie in the (100) plane and

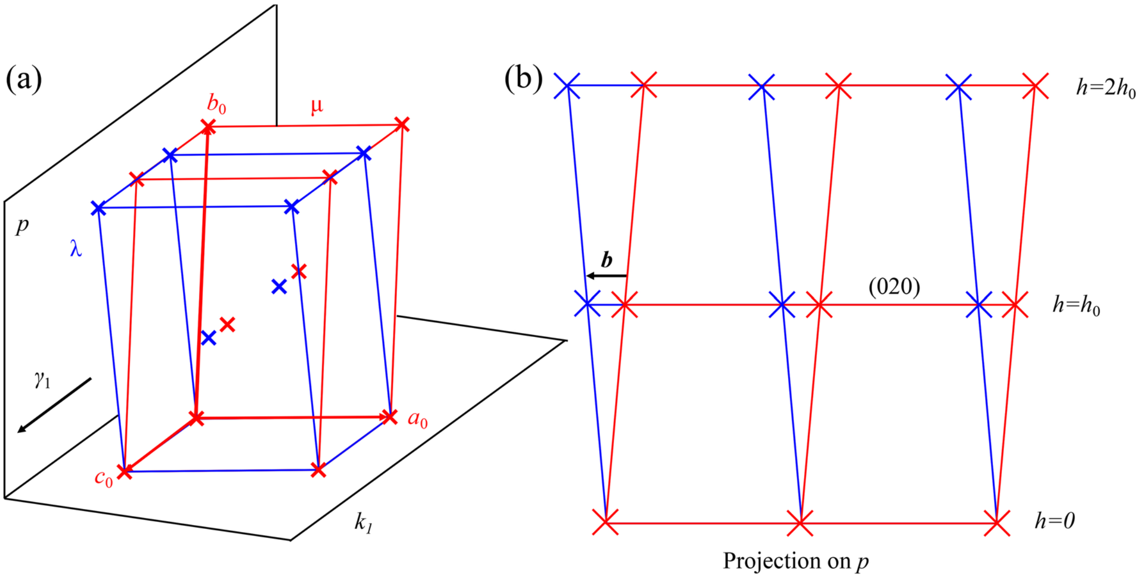

Fig. 8 **a** The CDP for the ideal case when ***b*** is parallel to [001]. **b** The CDP projected normal to the plane of shear p=(100)

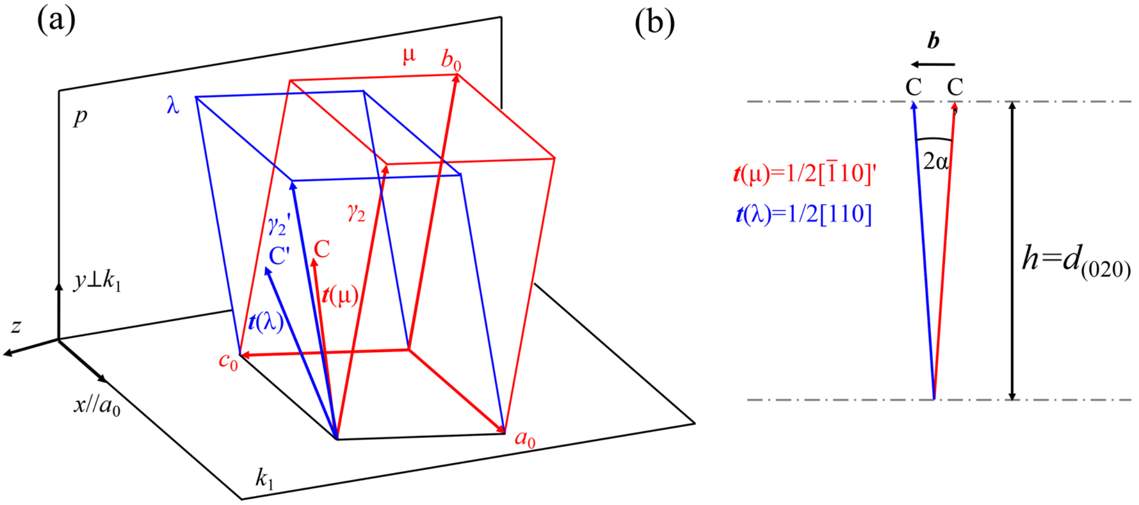

Fig. 9 **a** An axonometric view of the CDP for plagioclase. The bottom plane is the k_1 plane, and the back plane is the plane of shear p. The translation vectors and the twinning elements γ_1 and γ_2 are shown. The twinning elements γ_1 and γ_2 lie in the plane p. **b** The projection of the translation vectors on the plane of shear p. The angle between translation vectors is the rotation tilt angle of the wall in the type-II twin. The Burgers vector ***b*** and step height h are depicted

the determination of ***b*** is straightforward. In the actual case, Table 1, ***b*** is close to $[\bar{1}08]$. Figure 9a shows an axonometric projection (Hartman et al. 2008) of the CDP of a type I albite twin in labradorite. Orthogonal axes (x, y, z), used to describe shuffle vector components, and crystal axes (a_0, b_0, c_0), are shown. The bottom plane drawn in black is the k_1 disconnection glide plane, (010). The background plane is the shear plane p, which contains the twinning direction γ_1 and the conjugate twinning direction γ_2. The lattice vectors in the μ and λ crystals are depicted in red and blue, respectively. The conjugate twinning directions γ_2 and γ_2' are also shown. The vectors $\boldsymbol{t}(\mu)$ and $\boldsymbol{t}(\lambda)$ are designated ***OC*** and **OC′**, respectively; the end points of these vectors are located at the face-centered lattice sites illustrated in Fig. 6c, d. Figure 9b is the projection of the ***t*** vectors on p. The ***b*** vector lies in the plane of the projection and the unit step height h is shown. Hence, the Burgers vector and step height are identified by this topographical analysis. All parameters are listed in Table 3.

Relative to Fig. 4, the angle $2\varphi = 86.1°$ and the angle $2\alpha = 7.8° = 7.8°$, Table 3. Therefore, there is an

Table 3 Topological parameters of albite twin in labradorite

$t(\lambda)$	½ $[\bar{1}10]_T$	d'_{020}	0.641 nm
$t(\mu)$	½ [110]	d_{020}	0.641 nm
b	[− 0.0504, 0, − 0.1370]	H	0.641 nm
$\|b\|$	0.0874 nm	b/h	0.136
2φ	86.1°	2α	7.8°

incompatibility when the two types of twins meet and there is a repulsion as two twins near intersection as manifested by the variation in the pattern of extinction in Fig. 3c and the narrowing of a twin tip as it meets another twin. Because the incompatibility is small, as indicated by the small angle α, the repulsion in the albite–pericline case is weaker than many other systems with large α values, such as *fcc* metals.

One can postulate that the generally observed tendency to see more type II twins in more anorthitic plagioclase, i.e., as the Ca content increases, is a consequence of solid solution hardening. That is, the strain fields of the Ca and Al "solutes" increase the activation energy for disconnection motion (i.e., the twin growth rate $\dot{G}$) to the degree that it causes a gradual transition from type I to type II as the more favored system.

Disconnections in recovered twins

The structure of deformation twins can be modified by recovery. Prior to recovery, the type I twin interface comprises disconnections with short heights (i.e., $h \le \sim 2h_o$) and (010) terraces, as shown for plagioclase, where the TDs are unit (i.e., $h = d$), in Fig. 10a. The strain fields that accompany these defects drive recovery. After dynamic or static recovery, macroscopically curved portions of twin boundaries contain a structure of terraces offset by large steps as shown in Fig. 10b. The large steps have small Burgers vectors, which minimize the strain energy (Hirth et al. 2016). We describe these as recovered deformation twins to distinguish them from annealing twins formed by a different mechanism during recrystallization or crystal growth (Fullman and Fisher 1951). For example, in a high symmetry crystal like *fcc*, recovery of deformation twins produces pure steps (i = 3) with zero Burgers vectors (Gong et al. 2017).

The TM provides a prediction of the step height of disconnections in recovered albite twins. The CDP in low albite viewed along a $[\bar{1}00]$ direction is shown in Fig. 11a. The Burgers vectors are projected (owing to the triclinic symmetry), but the projected lengths are proportional to b. The magnitudes of projected Burgers vectors are plotted for different values of h. The length of the net Burgers vector ($\boldsymbol{b}_{net}$) is smallest around the 8th layer. Hence, steps with $h = 8d$ (5.1 nm) have the minimum possible strain energy. The illustrations in Fig. 10 convey that recovery occurs by coalescence of unit disconnections into a square step configuration to reduce their attendant strain fields. This process requires emission of a lattice dislocation (emissary dislocation), with a compensating Burgers vector nearly equal to $-8\boldsymbol{b}$ into the matrix or the twin (Wang et al. 2009). The emission requires nucleation of the emissary dislocation, a thermally activated process, which is why it is a recovery process.

Shuffles for deformation twins in plagioclase

Knowledge of shuffle vectors is of interest in predicting activation energies for TD motion and whether diffusional relaxation is likely (short vectors) or less likely (long vectors).

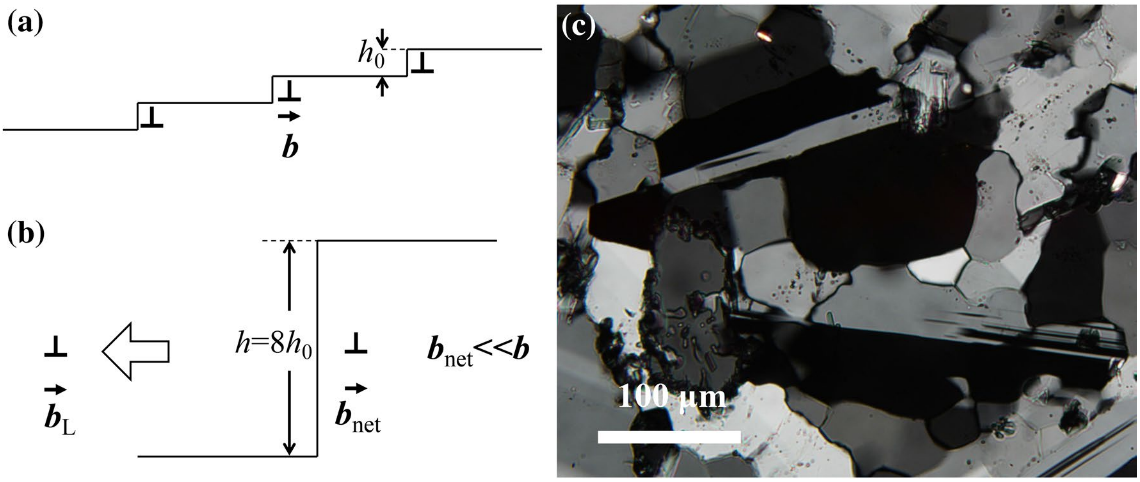

Fig. 10 **a** Unit disconnections on an as-deformed twin interface. **b** After recovery, the minimum strain-energy configuration has $h = 8h_0$. A lattice dislocation with Burgers vector b_L has been emitted to reduce the strain-energy. The net Burgers vector $\boldsymbol{b}_{net}$ is very small in this case. **c** Cross-polarized light micrograph of annealed albite sample containing recovered twins

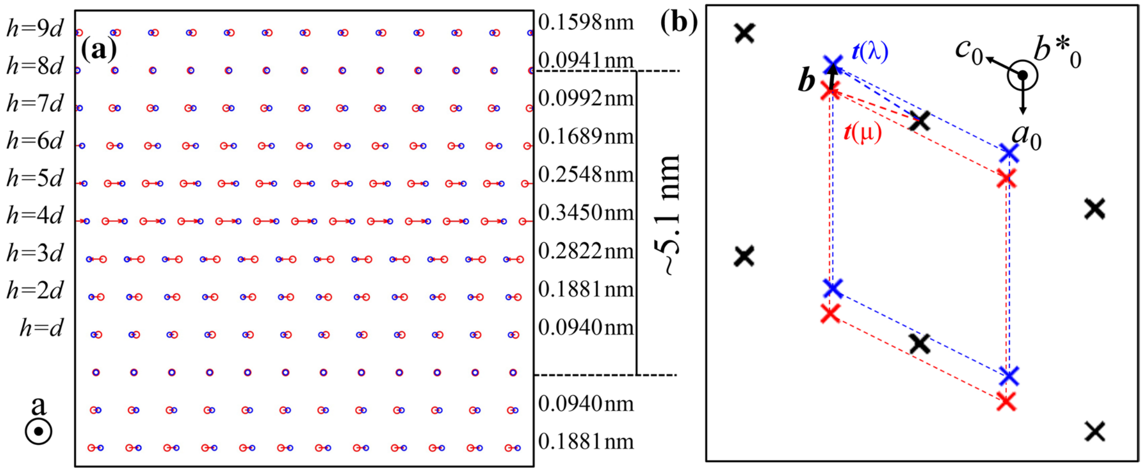

Fig. 11 **a** The CDP of low albite with the shortest Burgers vector labeled for each layer. **b** The b_0^* projection of CDP for the 8th layer. The Burgers vector is close to the [100] direction

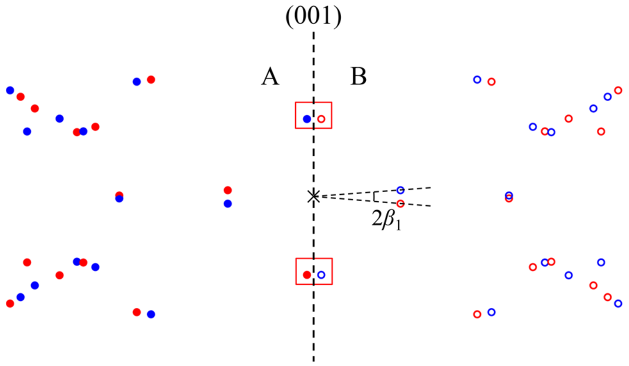

Fig. 12 The SDC of the structural group dipole formed by the superposition of Fig. 6b for both the matrix and the twin. The vertical line separates group A from group B. The rotation angle $2\beta_1$ is shown in this figure. This SDC is projected along the rotation axis of the dipole and parallel to the (010) plane. All Na, Al, Si and O atoms in group A are shown as hollow circles and those in group B as solid circles, respectively. The matrix atoms are red and the twin atoms are blue. The "swapping" oxygen atoms under and above the c–o–s are highlighted by two rectangles

We determine the shuffle vectors by identifying the shortest atomic displacements between twin and matrix according to Eq. (3). For disordered plagioclase, Ca and Na atoms occupy the same type of sites and Al and Si atoms occupy the same type of sites. For low albite, these elements are ordered.

For simple crystal systems, such as *hcp*, the CDC is sufficient to illustrate the shear and shuffle vector of twinning (Gong et al. 2019; Pond et al. 2016). However, the displacements in the CDC contain both shuffle and shear components which impede the straightforward visualization of shuffle vectors in complicated crystal structures. To solve this problem, the shifted dichromatic pattern (SDC) in which only shuffle displacements are shown is constructed as described in Hirth et al. (2019). The matrix is sheared by γ in accord with Eq. (3). With the shear displacements removed, the SDC is then created by forming a dichromatic complex of the sheared matrix and the twin. The remaining displacements required to match the sheared matrix to the twin comprise shuffles. Shuffles have been analyzed for simple metals but not for complex minerals. They are predicted here for albite by analyzing shuffle displacements for a single structural group, which then yields all displacements via symmetry operations. Shuffles can be envisioned to occur in two stages. First, while the centers-of-symmetry of the dipoles are in proper position after shear, each individual structural group must undergo additional rotation to satisfy mirror symmetry. They must be displaced (shuffled) equally and oppositely in the y direction, resulting in a dipole rotation of $-2\beta_1$ as shown in Fig. 12. After this, all atoms other than Na are not in the proper positions required by the twin symmetry and must undergo shuffles additional to those imparted by the rigid rotation.

The shuffles are determined for one structural group A, Fig. 6c. Those for group B and those at all other lattice sites then follow from symmetry operations. The details of the total shuffles in structural group A are depicted in the SDC of Fig. 13a–c which show separately the shuffles of Na, Al–Si, and O atoms. The shuffles in structural group B follow from the inversion symmetry. The coordinates of the crystal and the orthogonal system are shown on the side of Fig. 12. The SDC is viewed along the normal to the (010) twin plane (b* direction) and the [100] direction, as shown in the upper and lower figures, respectively. These two perpendicular directions give the planar-view and edge-on view of the twin plane. The shuffle vectors are labeled at the tips of the displacement arrows. We

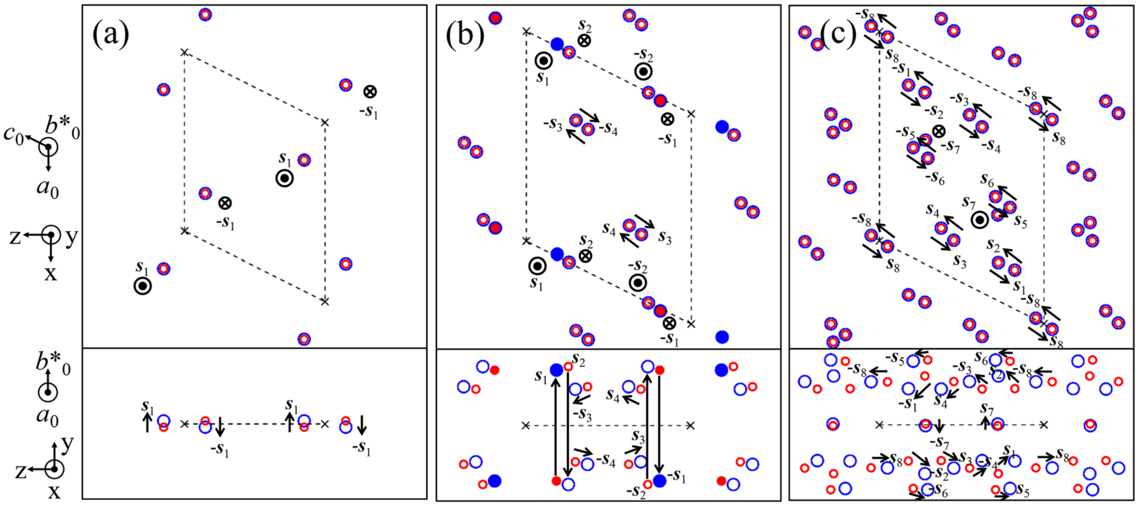

Fig. 13 **a**–**c** The SDCs for Na, Al, Si, and O atoms, respectively. The Al and Si atoms are represented by solid and open symbols, respectively, in **b**. The shuffle vectors are those for group A in Fig. 11. The shuffles of points in group B have the same magnitude but opposite direction in accordance with the point group symmetry. Two vectors for Si and Al, respectively, are much larger than the rest

Table 4 The rotational shuffle vectors of Na atoms accompanying disconnection motion in one structural group

Displacements	x	y	Z	Magnitude
s_1	0.0000	0.0288	0.0000	0.0288

The unit of distance is nm

Table 5 The shuffle vectors of Si and Al atoms accompanying disconnection motion in one structural group

Displacements	x	y	Z	Magnitude
s_1	0.0000	0.4300	0.0000	0.4300
s_2	0.0000	−0.4574	0.0000	0.4574
s_3	0.0351	0.0098	−0.0472	0.0596
s_4	−0.0351	0.0098	0.0472	0.0596
s_1^*	−0.0316	−0.0137	0.0460	0.0575
s_2^*	0.0316	−0.0137	−0.0460	0.0575

The unit of distance is nm. The vectors s^* represent shuffles to antisite positions

Table 6 The shuffle vectors of O atoms accompanying disconnection motion in one structural group

Displacements	x	y	Z	Magnitude
s_1	0.0288	0.0494	−0.0640	0.0858
s_2	−0.0288	0.0494	0.0640	0.0858
s_3	0.0471	−0.0291	−0.0490	0.0739
s_4	−0.0471	−0.0291	0.0490	0.0739
s_5	0.0418	0.0046	−0.0566	0.0705
s_6	−0.0418	0.0046	0.0566	0.0705
s_7	0.0000	0.0063	0.0000	0.0063
s_8	0.0431	0.0000	−0.0636	0.0769

The unit of distance is nm

determined the shuffle vectors from Eq. (4) utilizing the SDC.

The Na atoms (and the structural groups) undergo the purely rotational shuffles noted in Table 4, with components only in the y-direction. The shuffles of all other atoms are listed in Tables 5 and 6. For all O atoms and some Si and Al atoms, these shuffles are small, of the order of 0.05 nm. Hence, these should move relatively rapidly, analogous to the small shifts observed in a computer simulation of the relaxation of a perfect twin plane in albite (Li and Knowles 2013). The exception is the pair of Al and Si atom shown in the detail of a structural group in Fig. 14. These shuffles have an order of magnitude greater length, as indicated. At lower temperatures or shorter times, this exchange is suppressed and the Al–Si pair remains as an anti-site defect as described in Appendix 1. The corresponding anti-site shuffles are identified in Table 5 as s^*. These are small, of the same order as the other shuffles. In the unrelaxed configuration, the configuration would be a pseudo-twin (Smith 1974). The relaxation of the Al–Si pair should have an activation energy similar to that of self-diffusion. However, the mechanism is not simple, with resemblance to ring diffusion, since the relaxation motion is coupled. The importance of the Al–Si pair in disorder was noted early on by Laves (1952a, b). The disconnection model in Fig. 14 supports the Laves proposal. These

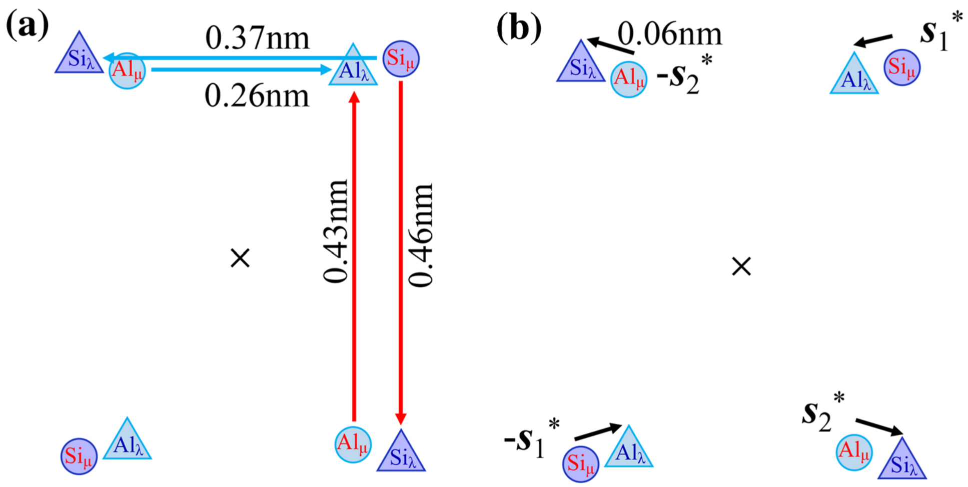

Fig. 14 **a** An SDC showing the large shuffle vectors for Si and Al from Fig. 9. **b** The short shuffle vectors create anti-site positions. These short vectors are labeled ***s**** in Table 5. (Hirth et al. 2019)

observations indicate that while other shuffles can influence the activation energy for disconnection motion, the Al–Si pair should limit the relaxation, leaving a pseudo-twin prior to recovery.

One other shuffle pair in Fig. 13 is unique. Most shuffles in Fig. 13 entail A–A and B–B displacements. However, motion of the O pair situated above and below the center-of-symmetry in Fig. 13 entails paired A–B and B–A shuffles. These structural groups are exchanged as described in Appendix 1. While these have no consequences structurally, they are important in the detailed motion of a disconnection. In this regard, the details of the atom motions as a disconnection moves are not simple. The shuffles certainly cannot occur simultaneously, which would lead to an inordinately large activation energy. Also, since the Al–O and Si–O bonding is strong, the polyhedra of oxygens that are nearest neighbors of Al or Si must tend to move as a unit. An atomistic simulation, which would reveal the actual details, would be valuable.

TEM observations of defects on twin boundaries

Experimental details

TEM samples were prepared from FIB lift-outs of polished sections. Before using the FIB, samples were gold coated to avoid charging of the surface and improve the image quality in dual-beam system. The TEM specimens were prepared with FEI Helios 660 Dual-beam system. The samples were extracted with an ion beam voltage of 30 kV and then final polished with 5 kV. TEM observations were performed in an FEI Tecnai Osiris operated at 200 kV.

Deformation twins in labradorite

The albite twin in labradorite was imaged in HRTEM. Figure 15a shows a bright field image, showing two twin boundaries. The diffraction patterns are collected from multiple directions, as shown in Fig. 15c–e, with the zone axes along [001], [102], and [100], respectively. The (020) spots from the twin and matrix overlap, and other spots have mirror symmetry relative to the (020) plane, verifying that the band is an albite twin. Figure 15b shows an HRTEM image taken with the electron beam parallel to the [100] direction, revealing four steps along a twin boundary. The height of these steps is equal to the d-spacing of (020) planes, corresponding to a unit disconnection according to the topological analysis discussed previously. These structures indicate that the growth of a type I twin (i.e., an albite twin) is accomplished by the glide of unit TDs on the twinning plane.

TEM characterization was also performed on the pericline twin (type II). The bright field image in Fig. 16a shows two twin boundaries. The selected area electron diffraction (SAED) pattern presented in Fig. 16c was taken with the electron beam parallel to [010], revealing an identical pattern for the twin and the matrix, consistent with the 180° rotation about the $[0\bar{1}0]$ direction, relative to the matrix, for a pericline twin. To identify steps, we collected SAED patterns from the $\left[\overline{11}0\right]_{\mathrm{M}}\left\|\left[1\bar{1}0\right]_{\mathrm{T}}\right.$ and $\left[\bar{1}00\right]_{\mathrm{M}}\|[100]_{\mathrm{T}}$ directions as shown in Fig. 16d, e. In addition to the split spots from the perfect crystals of the matrix and the twin, there are added satellites spots which have been well documented in previous studies (e.g., McLaren and Marshall 1974). These can arise from double diffraction or from ordering, but they do not affect our analysis and are not considered further. These two pairs of directions are not parallel to each other because of the rotation 2α that accommodates the incompatibility. The

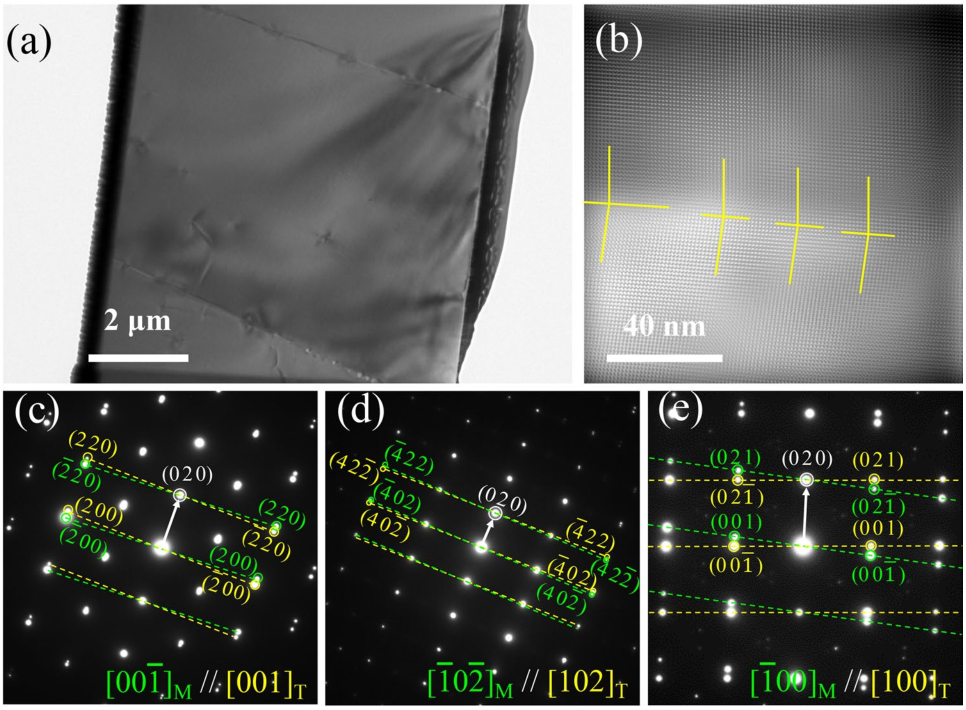

Fig. 15 **a** A bright field image of labradorite showing an albite twin. **b** An HRTEM image of albite twin boundary containing multiple unit steps. **c**–**e** SEAD patterns of the twin boundary taken from [00$\bar{1}$], [$\bar{1}$0$\bar{2}$], and [$\bar{1}$00 00] directions. The subscripts in these and the following figures indicate: T-twin, M-matrix, A and B, grains

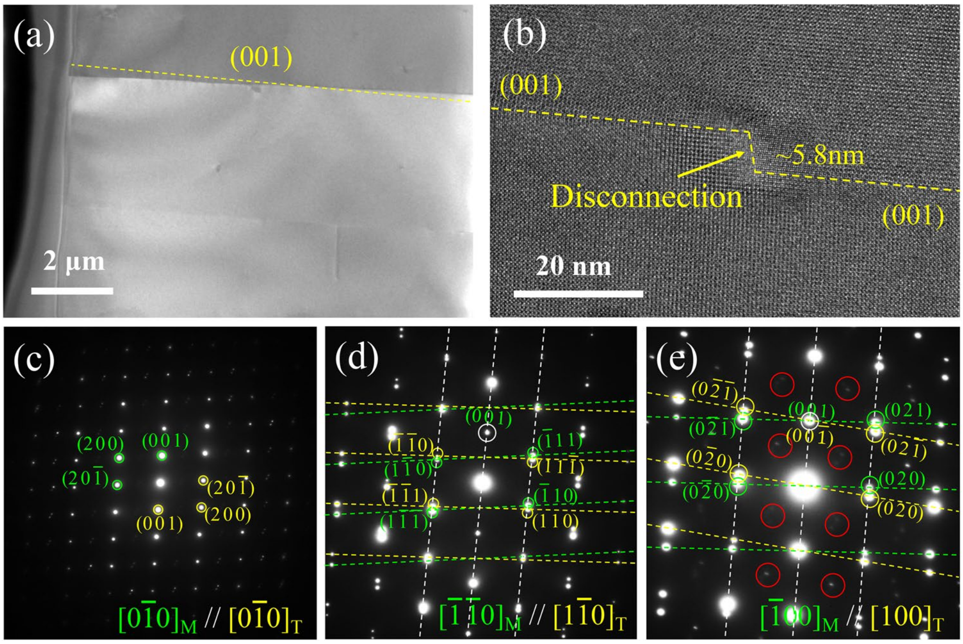

Fig. 16 **a** The bright field image of labradorite showing a pericline twin. The dashed line in **a** indicates the (001) plane according to the SEAD in **c**. **b** An HRTEM image of pericline twin boundary containing a big step. This accounts for the deviation of (001) plane in **a** from (001) plane in **b**. The center part of the step became amorphous because of radiation damage under the electron beam. **c**–**e** SEAD patterns of the twin boundary taken from the [0$\bar{1}$0], [$\bar{1}\bar{1}$0], and [$\bar{1}$00] directions

bright field image in Fig. 16a was collected in the same area as Fig. 16e. The trace of the twin boundary is perpendicular to the vector from the center spot to that of the (001) plane in Fig. 16e, which means that the twin boundary is close to the (001) plane. The HRTEM image in Fig. 16b was taken from a [100] direction, also revealing that the twin plane is near to a (001) plane. But a perfect (001) plane would not be stress free for a type-II twin. The equilibrium type II twin plane should be irrational with the index ($\bar{1}$, 0, 38.3), which is inclined to the (001) plane by 1.5°. Measurements of the inclination angle from the images range from 1° to 2°. Thus, agreement of the TM with the observation is good. Some scatter is expected in measurements at this scale, since extrinsic defects can be present on the boundary.

In general, a perfect k_2 boundary of a type II twin would comprise closely spaced dislocations forming a high-angle tilt wall. In the present case, the tilt wall in Fig. 16 is close to the (001) plane. This suggests that in order to lower the interfacial energy, the ($\bar{1}$, 0, 38.3) plane should decompose into a zig–zag structure, forming (001) facets separated by disconnections with small step heights, as indicated by the structure in Fig. 16b. Facet formation would not introduce long-range stresses, but there could be local stresses near the facet ends. The Burgers vector of these disconnections is irrational and has a large component of 0.2087 nm in the (001) plane and a small component normal to it. Like transformation disconnections in phase transformations, these defects are glissile in the (001) plane. Propagation of these defects advances the ($\bar{1}$, 0, 38.3) K_1' twin plane. Hence, although such a disconnection could not nucleate to produce a type I twin because of its large self-energy, it can form as a product of the type II mechanism. The presence of disconnections on the k_1 plane for a type I twin increases the strain energy and hence the total free energy. In contrast, the presence of disconnections on the k_2 plane for a type II twin decreases coherency strains (i.e., incompatibility) and lowers the free energy. The HRTEM image in Fig. 16b shows a disconnection with a height of 5.8 nm separating two (100) terraces. This large step could form as in Fig. 10 by the glide association of unit disconnections.

Recovered twins in low albite

We also characterized recovered deformation twins in the low albite specimen. HRTEM images and diffraction patterns are shown in Fig. 17a, c. In the diffraction patterns, the (020) spots overlap. The diffraction patterns and lattice fringes exhibit mirror symmetry relative to the (020) plane, a typical characteristic of a type-I twin. Figure 17a, b shows the albite twin boundary as observed along the [100] direction, revealing a band parallel to the twin boundary. The width of the band is about 5 nm. The band probably is associated with a step that is not parallel to the beam direction. When the beam is along [10$\bar{1}$], the band feature disappears, implying that the step is parallel to [10$\bar{1}$]. Figure 17d shows a [10$\bar{1}$] HRTEM image at higher magnification. In the center of the image, the bright area was amorphized by electron radiation damage. The level of the twin boundary is different on the two sides of the amorphous area, which means that there was a step in this amorphous area. The steps on the twin boundary have higher energy and can be amorphized more easily. The height of this step is measured to be 5 nm. From these observations, we conclude that there is a step with height of 5 nm in nearly the [100] direction on a recovered type I albite twin boundary. The existence of this step is consistent with the recovered step predicted from the coherent dichromatic pattern in Fig. 9. These large steps are sessile with respect to glide. They can only move by extensive diffusion-like shuffles, or by disconnection pair nucleation on the step riser (Pond et al. 1999; Wang et al. 2014)

Albite–Carlsbad twin

Another kind of boundary is shown in the TEM image and SEAD patterns in Fig. 18a, b. For this boundary, the (020)

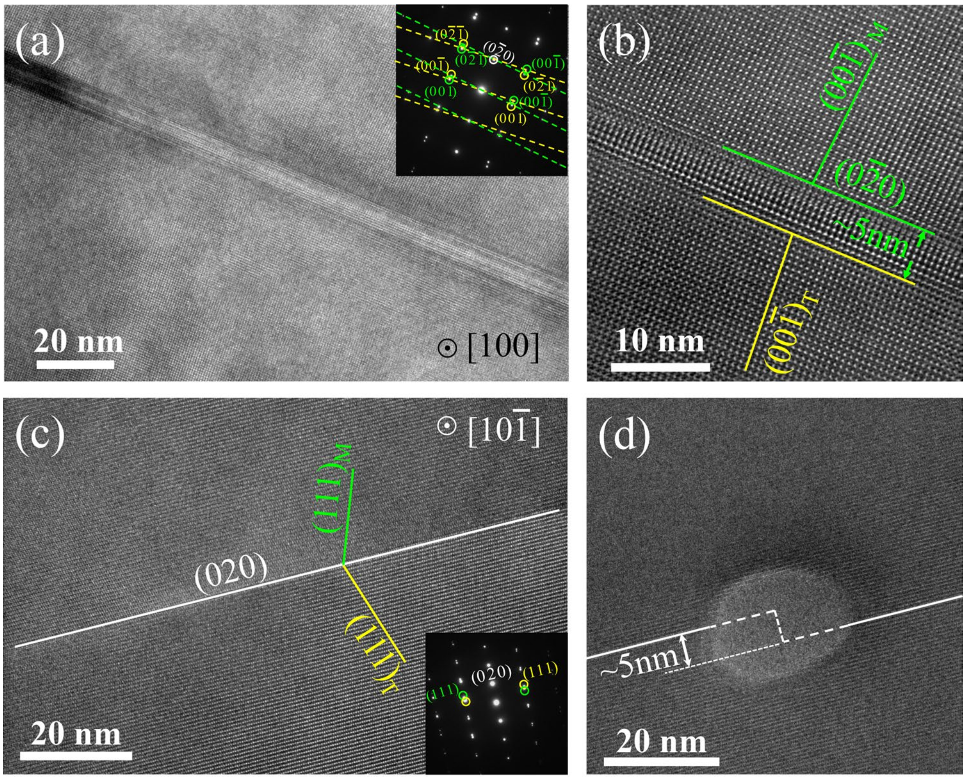

Fig. 17 **a** An HRTEM image of albite twin boundary in low albite showing a bright band. The insertion is a SEAD pattern of this area, collected along a [100] direction. **b** Magnified HRTEM image of the boundary in **a**. The bright band has a width of 5 nm. **c** HRTEM image of the twin boundary, with a SEAD pattern, collected along a [102] direction, inserted. **d** Magnified HRTEM image of the boundary in **c** showing a step with height of 5 nm. The center part of the step is amorphous

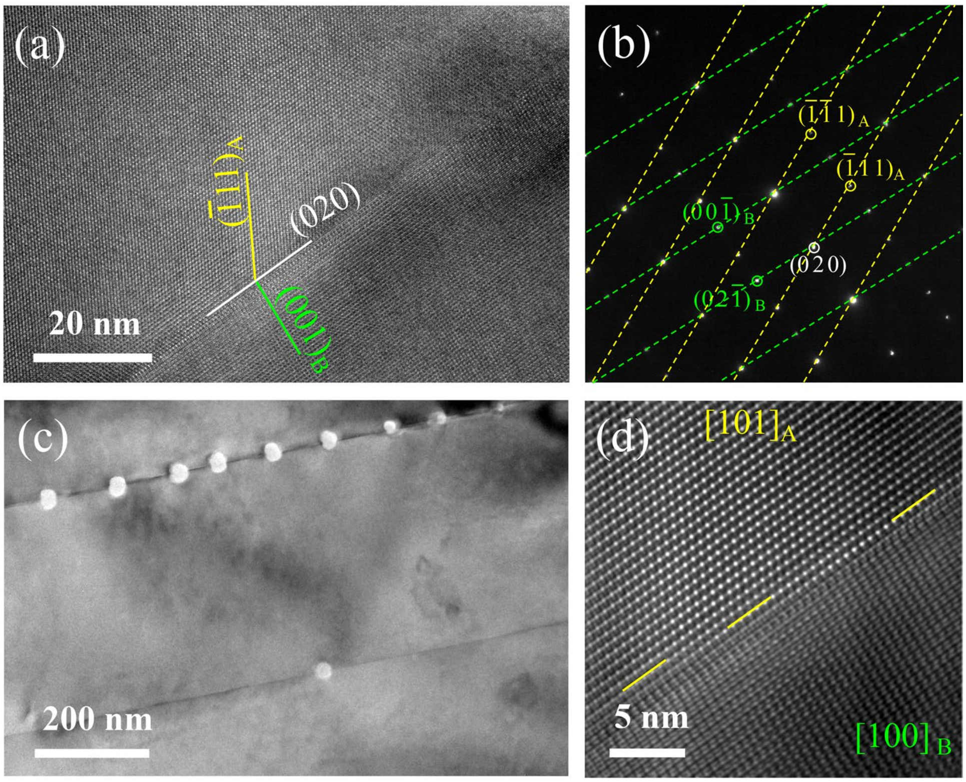

Fig. 18 **a** HRTEM image of a boundary showing an "Albite–Carlsbad twin" in low albite. **b** The SEAD pattern of this boundary. **c** A bright field image of the Albite–Carlsbad twin showing periodic amorphous spots on the boundary. **d** Magnified HRTEM image showing unit steps. **a**–**c** Taken from $[101]_A$ and $[100]_B$ direction

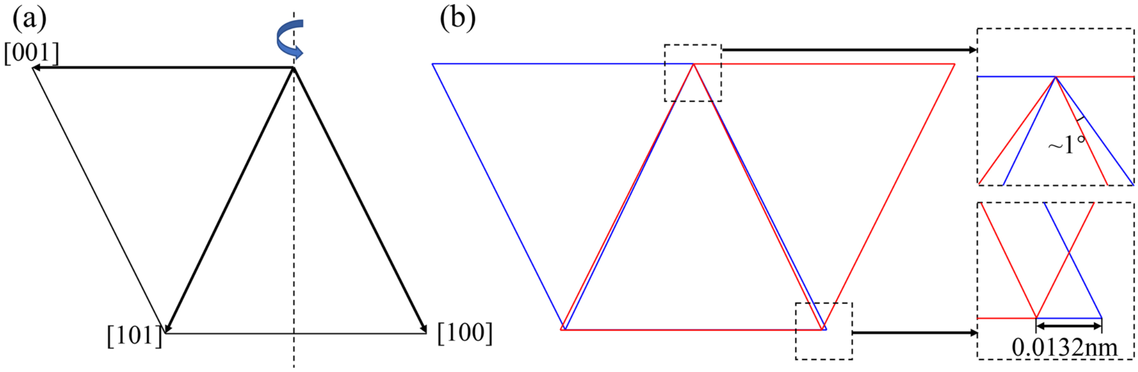

Fig. 19 **a** View of the (010) plane showing a rotation operation that produces the Albite–Carlsbad twin. **b** The overlapped (010) plane of matrix and twin crystals at an Albite–Carlsbad twin boundary. This figure shows the incompatible misfit, which must be accommodated by misfit dislocations

diffraction spots overlap. The diffraction patterns reveal that the orientation relationship (OR) is $(020)_A \Big\| \left(0\bar{2}0\right)_B [1001]_A \Big\| \left[00\bar{1}\right]_B$. This OR can be obtained by a 180° rotation around an axis perpendicular to both the normal to the (010) plane and the [001] direction. The latter alone would be a Carlsbad twin, possibly with a (100) twin plane (Smith and Brown 2012). Alternatively, a 180° rotation around the normal of (010) plane plus a 180° rotation around the [001] direction can lead to the same OR. The operation is illustrated in Fig. 19a. In mineralogy, these two steps of rotation corresponded to those that are characteristic of an albite twin and a Carlsbad twin, respectively. However, the interface is formally a grain boundary rather than a twin since it does not have twin symmetry at any interface (Laves 1952a, b; Smith and Brown 2012). The structure can be produced by double twinning or twinning plus slip that produces a grain boundary at the interface (Smith and Brown 2012). This dual nature is why it is called an Albite–Carlsbad twin, but this terminology is regarded aa improper (Laves et al. 1974). A better terminology would be a deformation band.

After illumination in the electron beam for several minutes, periodic amorphous spots appeared on the upper boundary in Fig. 18c. As shown in Fig. 19b, the lattice for two sides of this grain boundary has a small mismatch which should be accommodated by periodic grain-boundary disconnections. The HRTEM image in Fig. 18d is taken from this boundary and shows unit grain-boundary disconnections on the boundary decorated by amorphous regions arising from electron beam irradiation damage. Because of the strain field of these disconnections, the nucleation of the amorphous phase is more likely there. The mobility of these sorts of defects can accommodate creep by grain-boundary sliding mechanisms (Han et al. 2018). The observation of disconnections on this grain boundary, together with their presence in type-II twinning, is important, demonstrating that all types of deformations twins, as well as related structures with grain boundary disconnections, can translate in accordance with the TM. In some cases, the disconnections have large steps and many shuffles, so that the TD mobility might be quite limited or may require climb.

Discussion

The HRTEM observations of type-I albite and type-II pericline deformation twins are consistent with the predictions of the topological model. The same disconnections describe both types of twins. This result was unexpected and may be novel. However, it demonstrates a way in which a single disconnection system can produce two of the five deformation systems needed to satisfy the von Mises requirement, essentially because rotation and strain are separate mechanisms. Unit twinning disconnections are observed on some of the interfaces, indicating that twin growth occurs by motion of these defects. Also seen are disconnections with larger step height and reduced dislocation content. These must have formed by dynamic or static recovery. The recovery mechanism involves ejection of emissary dislocations from the boundary. The recovered twin defects are sessile with respect to glide and pin the interface under unloading or reverse loading. This result is parallel to the observations in metals with simpler crystal structure. The only difference is that the metal atoms are replaced by structural groups. We anticipate that deformation twinning in other minerals can be explained by similar mechanisms.

Extensive studies in metals show unequivocally that the mechanism of deformation twin growth is by the motion of twinning disconnections (called twinning dislocations in older literature), see the reviews: Christian and Mahajan (1995), Kelly and Knowles (2012) and Hirth et al. (2016). Nicolas et al. (1977) suggested that twinning in minerals occurred by a TD mechanism but this was questioned (Smith and Brown 2012). Our observations demonstrate that a TD mechanism described by the TM applies for albite and pericline twins. There is no other mechanism that can explain all observations.

The observation and characterization of deformation twins can be used to constrain the magnitude paleostress and the heterogeneity of stress state in natural rocks (e.g., Rowe and Rutter 1990). Twinning can be promoted by tectonic deformation, impact processes, thermal stresses, and the stress concentrations around fractures and fault zones. In many of these deformation environments, the microstructural constraints on differential stress are not straightforward to apply. For example, grain size application of grain size piezometry requires documentation of the activation of nominally steady-state dislocation creep. The analyses we present here provide a framework through which to investigate twinning in both laboratory and natural samples. Grain boundary sliding can also be accommodated by motion of disconnections (Han et al. 2018), such as those we document in Fig. 19, suggesting new ways to investigate creep behavior at conditions where grain boundary sliding mechanisms have been interpreted in plagioclase-rich lithologies (e.g., Miranda et al. 2016), as well as other geologic materials (e.g., Hansen and Warren 2016; Warren and Hirth 2006).

Conclusions

HRTEM observations support the predictions of the topological model for deformation twinning. Type I albite twins and type II pericline twins grow by the glide of unit twinning disconnections. The disconnection characteristics are determined. Calculated twinning shears agree with classical values. A method of determining shuffles from structural groups of atoms simplifies their determination.

Both the albite and pericline twins grow by the glide of the same disconnections, producing a conjugate twin pair. Hence, the same disconnection supplies two of the five systems needed to satisfy the von Mises requirement. Incompatibilities at Albite–Pericline intersections result in mutual repulsion between the two.

In addition to unit disconnections, both types of twin reveal disconnections with larger step heights and reduced dislocation content. These form by dynamic or static recovery and tend to pin the boundaries.

Acknowledgements The authors are pleased to acknowledge helpful contributions by R.C. Pond. Xie and Wang acknowledge support from the US National Science Foundation (NSF) (CMMI-1661686). Greg Hirth acknowledges support from NSF: EAR-1624178.

Appendix 1: Lattice site and atom exchanges

Almost all Burgers vectors in twins connect prefect lattice sites that are perfect translational ***t*** vectors in dichromatic spaces. However, there are a few cases where the vectors shear and shuffle to alternate sites in a process called synchroshear (Kronberg 1957). A better term is synchroshuffle, since the displacements are not the long-range ones defined by the Burgers vector. These are not perfect displacement vectors and create a special type of imperfect dislocation or disconnection. Examples of synchroshuffle include twinning, e.g., in alumina (Kronberg 1957), and phase transformations, e.g., in spinel (Poirier 1981) and Laves phases (Hazzledine and Pirouz 1993). The synchroshear displacements are of two kinds, knock-on and coupled pairs (Anderson et al. 2017). Synchroshear usually occurs in crystals with a basis, i.e., a structural group of atoms, or in simple structures a pair of atoms, at a lattice site that has point-group symmetry. For example, with a basis of 2, the dipole groups can be labeled as A and B. For more common cases, the shuffle or shear exchanges are A–A and B–B. For the synchronous cases the exchanges are A–B and B–A. To maintain stoichiometry there must be equal numbers of A–B and B–A exchanges. There are analogous displacements that we describe as anti-site exchanges. These arise during disconnection motion and entail atoms shuffling (or, less likely shearing) to the wrong site chemically. Again, there must be balanced A–B and B–A shifts.

Synchroshuffle was applied to twinning in alumina in the original work of Kronberg (1957). Often in twinning, the displacements are similar synchroshuffles. In twinning, the synchroshear/shuffle constraints often can be partly relaxed, as illustrated in the main text. For example, in a simulation of $(10\bar{1}2)$ twinning in Zr (Khater et al. 2013), knock-on, B–A and B–A exchanges (called swaps) occur. However, since the shuffle vectors simply complete perfect vector displacements from matrix to twin, no added fault is created. Thus, the distinction as an exchange is not as important. However, the exchange is of interest with regard to the atomic mechanism of motion. In contrast, the anti-site shuffles are important since they create local disorder, corresponding to a disorder fault in the wake of a moving disconnection. We describe the fault as a disorder fault since there is no incorrect layer stacking as in a stacking fault.

References

Anderson PM, Hirth JP, Lothe J (2017) Theory of dislocations, 3rd edn. Cambridge University Press, Cambridge

At Santoro, Mighell A (1970) Determination of reduced cells. Acta Crystallogr Sect A Cryst Phys Diffract Theor General Crystallogr 26:124–127

Bevis M, Crocker A (1969) Twinning modes in lattices. Proc R Soc Lond A 313:509–529

Bilby BA, Crocker A (1965) The theory of the crystallography of deformation twinning. Proc R Soc Lond A 288:240–255

Christian JW, Mahajan S (1995) Deformation twinning. Prog Mater Sci 39:1–157

Frank F (1951) Crystal dislocations-elementary concepts and definitions. Phil Mag 42:809–819

Frank F (1953) A note on twinning in alpha-uranium. Acta Metall 1:71–74

Fullman R, Fisher J (1951) Formation of annealing twins during grain growth. J Appl Phys 22:1350–1355

Gong M, Hirth JP, Liu Y, Shen Y, Wang J (2017) Interface structures and twinning mechanisms of twins in hexagonal metals. Mater Res Lett 5:449–464

Gong M, Xu S, Xie D, Wang S, Wang J, Schuman C, Lecomte J-S (2019) Steps and $\left\{11\bar{2}1\right\}$ secondary twinning associated with $\left\{112\bar{2}\right\}$ twin in titanium. Acta Mater 164:776–787

Hahn T, Klapper H (2006) 3.3 Twinning of crystals. International tables for crystallography D. Springer, Netherlands, pp 393–448

Han J, Thomas SL, Srolovitz DJ (2018) Grain-boundary kinetics: a unified approach. Prog Mater Sci 98:386–476

Hansen LN, Warren JM (2016) Quantifying the effect of pyroxene on deformation of peridotite in a natural shear zone. J Geophys Res Solid Earth 120:2717–2738

Hardouin Duparc O (2017) A review of some elements for the history of mechanical twinning centred on its German origins until Otto Mügge's K_1 and K_2 invariant plane notation. J Mater Sci 52:4182–4196

Harlow GE, Brown GE (1980) Low albite- an X-ray and neutron diffraction study. Am Miner 65:986

Hartman NW, Bertoline GR, Wiebe EN, Ross WA (2008) Technical graphics communication. McGraw-Hill Education, New York, pp 577–578

Hazzledine P, Pirouz P (1993) Synchroshear transformations in Laves phases. Scr Metall Mater 28:1277–1282

Hirth J, Pond R, Hoagland R, Liu X-Y, Wang J (2013) Interface defects, reference spaces and the Frank–Bilby equation. Prog Mater Sci 58:749–823

Hirth J, Wang J, Tomé C (2016) Disconnections and other defects associated with twin interfaces. Prog Mater Sci 83:417–471

Hirth JP, Wang J, Hirth G (2019) A topological model for defects and interfaces in complex crystal structures. Am Mineral 104:966–972

Horst W, Tagai T, Korekawa M, Jagodzinski H (1981) Modulated structure of a plagiociase angz: theory and structure determination. Zeitschrift für Kristallographie Crystall Mater 157:233–250

Kelly A, Knowles KM (2012) Crystallography and crystal defects. Wiley, New York

Khater H, Serra A, Pond R (2013) Atomic shearing and shuffling accompanying the motion of twinning disconnections in zirconium. Phil Mag 93:1279–1298

Kronberg M (1957) Plastic deformation of single crystals of sapphire: basal slip and twinning. Acta Metall 5:507–524

Laves F (1952a) Phase relations of the alkali feldspars. II. The stable and pseudo-stable phase relations in the alkali feldspar system. J Geol 60:549–574

Laves F (1952b) Phase relations of the alkali feldspars: I. Introductory remarks. J Geol 60:436–450

Laves F, MacKenzie W, Zussman J (1974) Domain and deformation textures in plagioclase and their investigation by photo-emission-electron-microscopy (PEEM) and by transmission electron microscopy. Manchester University Press, Manchester, pp 536–550

Li B, Knowles KM (2013) Molecular dynamics simulation of albite twinning and pericline twinning in low albite. Modell Simul Mater Sci Eng 21:055012

McLaren A, Marshall D (1974) Transmission electron microscope study of the domain structures associated with the b-, c-, d-, e-and f-reflections in plagioclase feldspars. Contrib Miner Petrol 44:237–249

Mehl L, Hirth G (2008) Plagioclase preferred orientation in layered mylonites: evaluation of flow laws for the lower crust. J Geop Res 113:B05202

Miranda EA, Hirth G, John BE (2016) Microstructural evidence for the transition from dislocation creep to dislocation-accommodated grain boundary sliding in naturally deformed plagioclase. J Struct Geol 92:30–45

Mügge O (1889) Ueber homogene Deformationen (einfache Schiebungen) an den triklinen Doppelsalzen BaCdCl4. 4aq. Neues Jahrbuch für Mineral Geol Palaeontol Beilage 6:274–304

Nicolas A, Bouchez JL, Blaise J, Poirier JP (1977) Geological aspects of deformation in continental shear zones. Tectonophysics 42:55–73

Niggli P (1928) Krystallographische und strukturtheoretische Grundbegriffe. Akademische Verlagsgesellschaft MBH, Tübingen

Poirier J (1981) On the kinetics of olivine-spinel transition. Phys Earth Planet Inter 26:179–187

Pond R, Hirth J (2018) Topological model of type II deformation twinning. Acta Mater 151:229–242

Pond R, Serra A, Bacon D (1999) Dislocations in interfaces in the hcp metals—II. Mechanisms of defect mobility under stress. Acta Mater 47:1441–1453

Pond R, Ma X, Chai Y, Hirth J (2007) Topological modelling of martensitic transformations. Dislocations Solids 13:225–262

Pond RC, Hirth J, Serra A, Bacon D (2016) Atomic displacements accompanying deformation twinning: shears and shuffles. Mater Res Lett 4:185–190

Pond RC, Hirth JP, Knowles KM (2019) Topological model of type II deformation twinning in NiTi martensite. Phil Mag 99:1619–1634

Rowe KJ, Rutter EH (1990) Palaeostress estimation using calcite twinning: experimental calibration and application to nature. J Struct Geol 12(1):1–17

Smith JV (1974) Feldspar minerals: crystal structure and physical properties, vol 1. Springer, New York

Smith JV, Brown WL (2012) Feldspar minerals: crystal structures, physical, chemical, and microtextural properties, vol 1. Springer, Berlin

Stünitz H, Fitz Gerald J D, Tullis J (2003) Dislocation generation, slip systems, and dynamic recrystallization in experimentally deformed plagioclase single crystals. Tectonophysics 372 (3–4):215–233

Tullis J, Dell'Angelo LN, Yund RA (1998) Formation of ductile shear zones along former faults in feldspathic rocks. In: Snoke AW, Tullis J, Todd VR (eds) Fault-related rocks: a photographic atlas. Princeton Univ Press, Princeton, pp 252–253

Van Swygenhoven H, Derlet P (2008) Atomistic simulations of dislocations in FCC metallic nanocrystalline materials. Dislocations Solids Tribute FRN Nabarro 14:1

Wang J, Hirth JP, Tomé CN (2009) Twinning nucleation mechanisms in hexagonal close-packed crystals. Acta Mater 57:5521–5530

Wang J, Yu Q, Jiang Y, Beyerlein IJ (2014) Twinning-associated boundaries in hexagonal close-packed metals. JOM 66:95–101

Warren JM, Hirth JG (2006) Grain size sensitive deformation mechanisms in naturally deformed peridotites. Earth Planet Sci Lett 248:438–450

Wenk H-R, Bulakh A (2016) Minerals: their constitution and origin. Cambridge University Press, Cambridge

Xu S, Zhou P, Liu G, Xiao D, Gong M, Wang J (2019) Shock-induced two types of $\left(101\bar{2}\right)$ sequential twinning in titanium. Acta Mater 165:547–560

Yu Q, Wang J, Jiang Y, McCabe RJ, Li N, Tomé CN (2014a) Twin–twin interactions in magnesium. Acta Mater 77:28–42

Yu Q, Wang J, Jiang Y, McCabe RJ, Tomé CN (2014b) Co-zone $\left(1\bar{0}12\right)$ twin interaction in magnesium single crystal. Mater Res Lett 2:82–88

Zhu Y, Narayan J, Hirth J, Mahajan S, Wu X, Liao X (2009) Formation of single and multiple deformation twins in nanocrystalline FCC metals. Acta Mater 57:3763–3770